Trends in Downwelling Longwave Radiance over the Southern Great Plains

Lei Liu[1,1], Yi Huang[1,1], John Richard Gyakum[1], David D. Turner[2,2], P. Jonathan Gero[3,3], and John Richard Gyakum[1]

[1]McGill University
[2]NOAA Earth System Research Laboratory
[3]University of Wisconsin–Madison

November 30, 2022

Abstract

Downwelling longwave radiation (DLR) is an important part of the surface energy budget. Spectral trends in the DLR provide insight into the radiative drivers of climate change. In this research, we process and analyze a 23-year downwelling longwave radiance record measured by the Atmospheric Emitted Radiance Interferometers (AERI) at the Southern Great Plains (SGP) site of the Atmospheric Radiation Program. Two AERIs were deployed at SGP with an overlapping observation period of about 10 years, which allows us to examine the consistency and accuracy of the measurements and to characterize discrepancies between them due to undetected instrumentation errors. Using the 23-year record, we analyze the all-sky radiance trends in DLR, which reflects the associated surface warming trend at SGP during this same period and also the complex changes in meteorological conditions. For instance, the observed radiance in the CO_2 absorption band follows closely the near-surface air temperature variations. The changes in the sky fraction of clear-sky and thick cloudy-sky scenes offset the radiance changes in the window band. Our analysis shows that the radiance trend uncertainty in the DLR record to date mainly results from the climate internal variability rather than the measurement error, which highlights the importance of continuing the DLR spectral measurements to unambiguously detect and attribute climate change.

1

Trends in Downwelling Longwave Radiance over the Southern Great Plains

Lei Liu[1], Yi Huang[1], John R. Gyakum[1], David D. Turner[2], P. Jonathan Gero[3]

[1]Department of Atmospheric and Oceanic Sciences, McGill University, Quebec, Canada.

[2]NOAA/OAR/Global Systems Laboratory, Boulder, Colorado, USA.

[3]Space Science and Engineering Center, University of Wisconsin-Madison, Madison, Wisconsin, USA.

Corresponding author: Lei Liu (lei.liu5@mail.mcgill.ca)

Key Points:

- Long-term AERI measurements disclose distinctive DLR trends, demonstrating the advantages of the spectral data for climate monitoring.

- The changes in clear/cloudy sky fractions offset DLR changes caused by warming and increases in greenhouse gases.

- The radiance trend uncertainty mainly results from the natural variability, which emphasizes the need to continue the measurements.

18 **Abstract**

19 Downwelling longwave radiation (DLR) is an important part of the surface energy budget.
20 Spectral trends in the DLR provide insight into the radiative drivers of climate change. In this
21 research, we process and analyze a 23-year downwelling longwave radiance record measured
22 by the Atmospheric Emitted Radiance Interferometers (AERI) at the Southern Great Plains
23 (SGP) site of the Atmospheric Radiation Program. Two AERIs were deployed at SGP with
24 an overlapping observation period of about 10 years, which allows us to examine the
25 consistency and accuracy of the measurements and to characterize discrepancies between
26 them due to undetected instrumentation errors. Using the 23-year record, we analyze the all-
27 sky radiance trends in DLR, which reflects the associated surface warming trend at SGP
28 during this same period and also the complex changes in meteorological conditions. For
29 instance, the observed radiance in the CO_2 absorption band follows closely the near-surface
30 air temperature variations. The changes in the sky fraction of clear-sky and thick cloudy-sky
31 scenes offset the radiance changes in the window band. Our analysis shows that the radiance
32 trend uncertainty in the DLR record to date mainly results from the climate internal
33 variability rather than the measurement error, which highlights the importance of continuing
34 the DLR spectral measurements to unambiguously detect and attribute climate change.

35 **1 Introduction**

36   Longwave radiation is a key component of the atmospheric energy budget that drives
37 climate change. At the top of the atmosphere (TOA), the outgoing longwave radiation (OLR),
38 as well as its spectrally resolved radiance, is monitored by satellites with global coverage and
39 long-term records (e.g., Liebmann & Smith, 1996; Stephens et al., 2012). This allows us to
40 study the changes in OLR and to test climate models (e.g., Harries et al., 2001; Huang &
41 Ramaswamy, 2009; Huang, Ramaswamy, Huang, et al., 2007; Huang, Ramaswamy, &
42 Soden, 2007; Wielicki et al., 2002). Despite the continuous spatiotemporal coverage of OLR
43 spectra, the compensating effects of greenhouse gas opacity and temperature warming make
44 it difficult to detect climate change (Huang & Ramaswamy, 2009).

45   Downwelling longwave radiation (DLR) emitted by the atmosphere is one key
46 component in the surface energy budget (Stephens et al., 2012; Trenberth et al., 2009).
47 Compared to the radiation budget at the TOA, the surface radiation budget is more uncertain
48 and DLR is a main contributor to the uncertainty (Trenberth et al., 2009; Wild et al., 2012).
49 This is largely due to the lack of global and long-term observations of DLR. DLR
50 observations, especially spectrally resolved radiance, have been limited to specific locations.
51 Despite the limited records, it has been demonstrated that DLR measurements are useful for
52 understanding the surface energy balance and testing the climate models. For example, Lubin
53 (1994) explained the super greenhouse effect using the observed DLR spectra over equatorial
54 oceans; Feldman et al. (2015) used the DLR spectra to measure CO_2 radiative forcing at the
55 Southern Great Plains (SGP) and the North Slope Alaska sites; Shupe and Intrieri (2004),
56 Kapsch et al. (2016), Huang et al. (2019), Sokolowsky et al. (2020) and a number of others
57 diagnosed the DLR variability in relation to sea ice, clouds and other climate changes in polar
58 regions.

59   Climate change is driven by changes in energy balance. This leads us to an
60 overarching question regarding the surface energy balance: can climate change be detected
61 and understood by monitoring the DLR spectrum? One advantage of the DLR, compared to
62 the OLR, is that the compensating effects mentioned earlier vanishes. In the DLR, the
63 greenhouse gas opacity and temperature warming effects reinforce each other to increase
64 DLR. This makes DLR a potentially advantageous means for monitoring climate change

65   (Huang, 2013). The signals from different meteorological variables such as temperature,
66   greenhouse gases and clouds imprint different spectral signatures. This allows for a spectral
67   fingerprinting of their changes (Huang et al., 2010). At the SGP site, the fifth generation
68   European Centre for Medium-Range Weather Forecasts atmospheric reanalysis dataset,
69   ERA5 (Hersbach et al., 2020), shows that there has been a significant warming in surface air
70   temperature with a magnitude of ~0.045 K/year between 1996 and 2018 (Figure 1). Can this
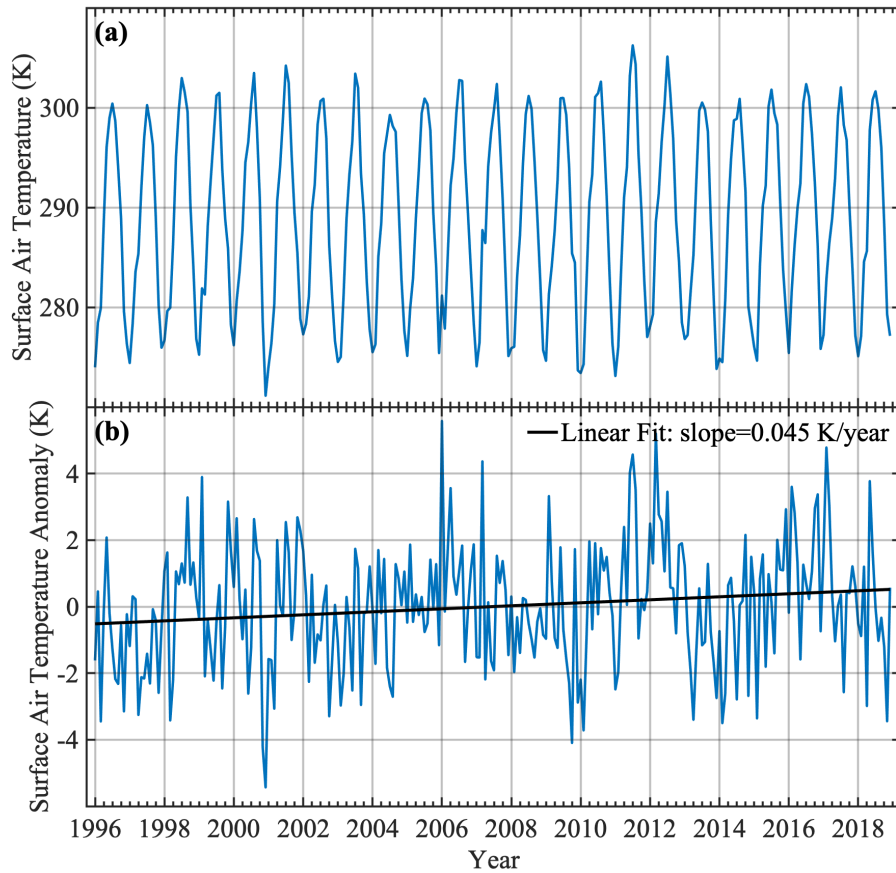71   warming be detected from the DLR spectral records?

Figure 1. Warming trend at SGP. Shown here is the ERA5 monthly mean 2-meter air temperature time series at the SGP site (average of nine 0.25°x0.25° resolution grid boxes centered at: 97.5° W and 36.5° N) between 1996 and 2018. The anomaly is defined with respect to multi-year monthly mean of each calendar month.

77   We have two primary objectives in this paper. First, we are interested in constructing
78   a long-term monthly DLR spectral record based on the 23 years of measurements by the
79   Atmospheric Emitted Radiance Interferometers (AERIs) installed at the SGP site of the
80   Atmospheric Radiation Measurement (ARM) program of the U.S. Department of Energy.
81   Two AERI instruments have been deployed at this site and have rendered 10 years of
82   overlapping observations but with different sampling strategies (e.g., 3 min sky average every
83   8 minutes vs multiple 20-s sky average observations every 4 minutes). We will examine the
84   accuracy and consistency of the measurements and validate them against synthetic spectra
85   simulated from collocated atmospheric measurements using a benchmark radiation model.
86   Second, we will show the analysis of the long-term DLR spectral trends measured by the two
87   AERIs for the period of 1996-2018. We are interested in whether the radiance trends are in
88   concert with the warming temperature trend (Figure 1). This work will also verify the trends
89   documented by Gero and Turner (2011) using the early years of the DLR record and analyze
90   the contributions from different sky conditions.

91 **2 Data and Methods**

92   2.1 AERI data processing

93   The AERI is a Fourier transform spectrometer that measures the DLR radiance
94 emitted from the atmosphere with good accuracy at high temporal and spectral resolution
95 (Knuteson et al., 2004a, 2004b). The measurements cover the spectral range between 520 and
96 3020 cm^{-1} with a resolution of 0.5 cm^{-1}. Two high-emissivity blackbodies, a hot blackbody
97 with a fixed temperature at around 60 degrees Celsius and another blackbody at ambient
98 temperature (Knuteson et al., 2004a), are used for radiometric calibration based on the
99 method of Revercomb et al. (1988). The long-term annual mean DLR spectra and the
100 standard deviation of DLR spectra for different sky types (classification method explained
101 later) at SGP site are shown in Figure 2. The main difference in DLR between different sky
102 types is primarily in the window portion of the spectrum (between 800 – 1200 cm^{-1}) shown in
103 Figure 2a. The standard deviation of thick cloudy-sky DLR is found to be the smallest among
104 all the different sky types in the window band (Figure 2b), which indicates small variability
105 of the radiating temperature of the thick clouds. We focus on the mid-infrared spectral range
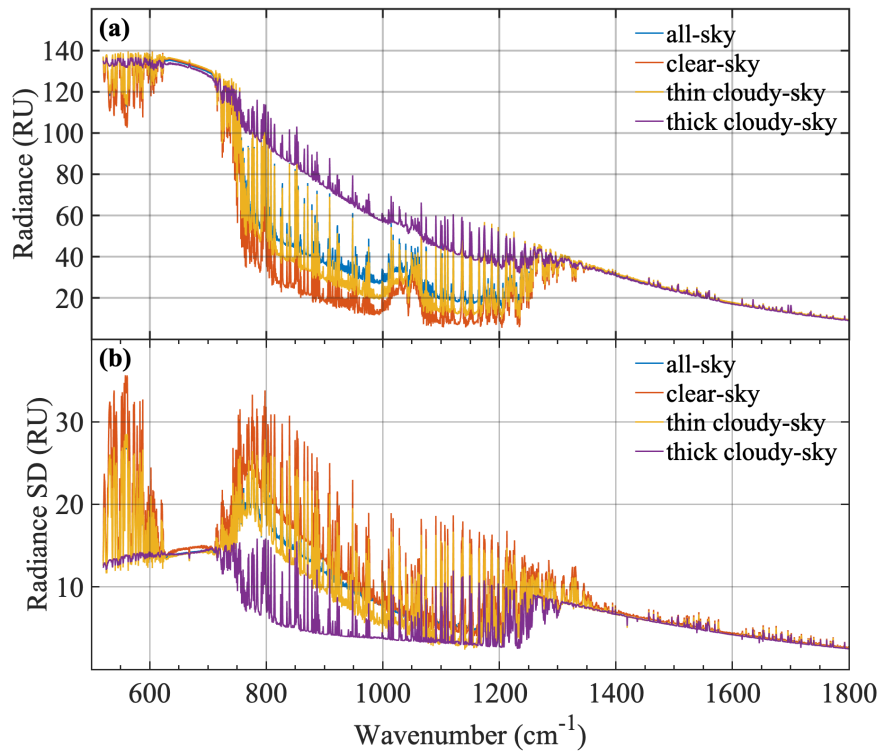106 from 520 to 1800 cm^{-1} in this paper.

107

108 **Figure 2.** (a) Annual mean AERI spectra for different sky types at SGP. (b) Standard
109 deviation of monthly mean AERI spectra for different sky types at SGP. (RU: Radiance
110 Units; 1 RU = 1 mW/(m^2 sr cm^{-1}))

111   The two AERIs deployed at SGP have different observational periods and different
112 sampling frequencies. AERI-01 operated from July 1995 to March 2014, while AERI-C1 has
113 operated from February 2004 to present. C1 is the current name of the Central Facility
114 location of SGP site which is used to be called E14, e.g. in Gero and Turner (2011). The two
115 AERIs were deployed virtually side-by-side (within 5 meters of each other). Given their field
116 of view (FOV) of 1.3 degrees, both instruments view essentially the same portion of the sky.

117 The overlapping observations make it possible to test the accuracy and consistency of the
118 measurements. However, the two instruments differ with respect to their sampling frequency.
119 AERI-01 measures one DLR spectrum approximately every 8 minutes; its measurement cycle
120 includes a 200-second sky-dwell period (Knuteson et al., 2004b) and the rest of the cycle is
121 used for viewing the blackbodies for calibration. AERI-C1 uses a rapid mode with a ~20-
122 second sampling cycles (Turner et al., 2006). Such differences in the measurements
123 necessitate appropriate procedures to homogenize the data from the two AERIs for inter-
124 comparisons and trend analyses.

125

126 **Figure 3.** Data processing flowchart. Yellow and purple squares represent AERI-01 and
127 AERI-C1 DLR data respectively. Blue squares represent important data processing steps.
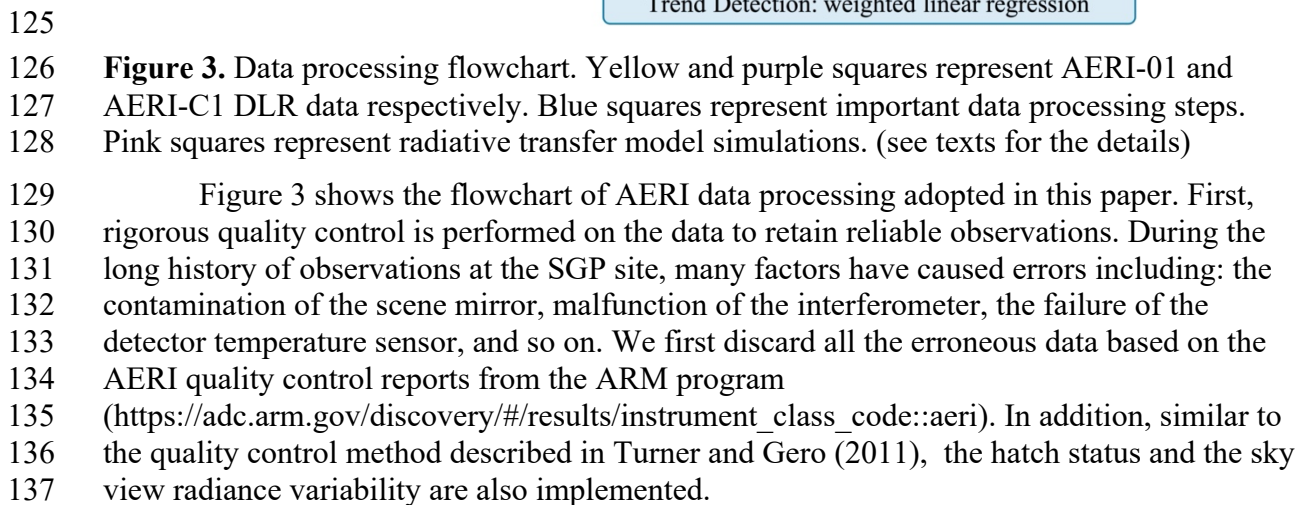128 Pink squares represent radiative transfer model simulations. (see texts for the details)

129 Figure 3 shows the flowchart of AERI data processing adopted in this paper. First,
130 rigorous quality control is performed on the data to retain reliable observations. During the
131 long history of observations at the SGP site, many factors have caused errors including: the
132 contamination of the scene mirror, malfunction of the interferometer, the failure of the
133 detector temperature sensor, and so on. We first discard all the erroneous data based on the
134 AERI quality control reports from the ARM program
135 (https://adc.arm.gov/discovery/#/results/instrument_class_code::aeri). In addition, similar to
136 the quality control method described in Turner and Gero (2011), the hatch status and the sky
137 view radiance variability are also implemented.

138   After the *Quality Control* step, we average the AERI-C1 spectra over 8-min intervals,
139   to be consistent with the AERI-01 sampling period. Then, in the *Sky Classification* step, we
140   apply a machine learning algorithm (detailed below) to classify the sky types (clear, thin and
141   thick clouds) based on the 8-min mean radiance spectra. Next, we take hourly averages of the
142   radiance data and verify proper diurnal sampling in each month to ensure no missing data for
143   any 24-hour period. Then the monthly mean spectra are obtained by averaging the 24-hourly
144   spectra of each day during the given month. Monthly means are discarded when the count of
145   hourly spectra is below 400 (~55%).

146   Some channels in the center of CO_2 absorption band (around 667 cm^{-1}) and water
147   vapor absorption band (1300 – 1800 cm^{-1}) in which the near-surface atmosphere is so opaque
148   that the channels are essentially uncalibrated are discarded based on the criterion that the
149   gaseous optical depth for a 1-meter layer of atmosphere at the surface is above 0.5 in the
150   *Optical Depth Screening* step. Finally, the monthly anomaly spectra are obtained by
151   subtracting the long-term monthly spectra of each calendar month (which effectively removes
152   the seasonal cycle). The results are illustrated in Figure 4. The long-term trends in the DLR
153   spectra are analyzed based on the monthly anomaly spectra with the help of synthetic clear-
154   sky DLR to differentiate the measurements of the two AERIs during the overlapping period
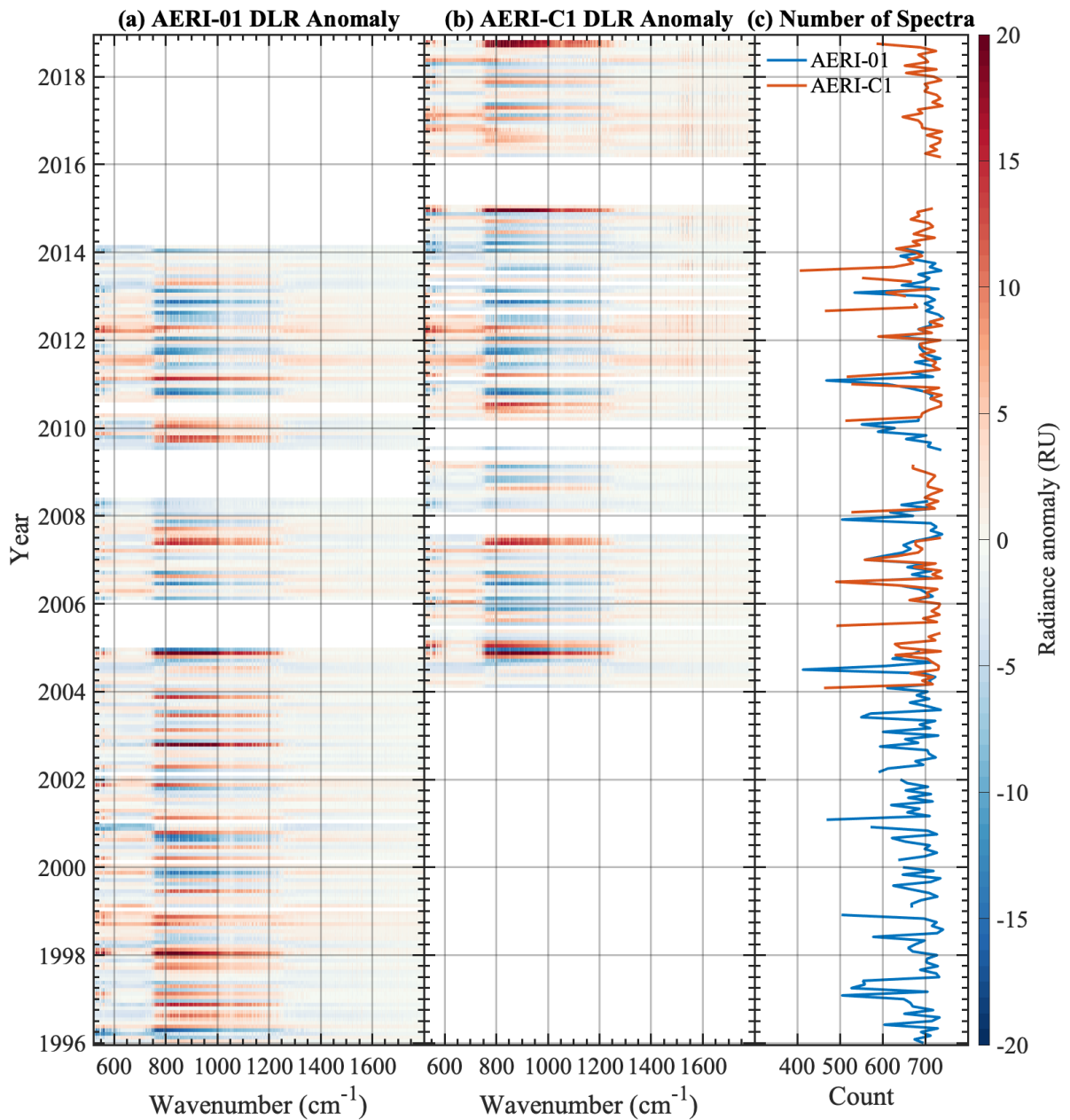155   using the method detailed in Appendix A.
156

Figure 4. Monthly anomaly of AERI-observed DLR spectra and hourly spectra count in each month.

In most months, the number of hourly mean spectra is larger than 700 (Figure 4c), which means the instruments operated for >95% of the time. The strongest monthly DLR anomalies are seen in the window band (800 – 1200 cm^{-1}). The pattern of the DLR radiance anomalies in the overlapping observational period is very similar between AERI-01 and AERI-C1.

2.2 Sky classification

Clouds strongly influence the DLR flux and spectra, especially in the atmospheric window (800 – 1200 cm^{-1}). In order to identify the causes of the DLR trends, we separate the clear-sky spectra from the cloudy ones and to examine their trends separately.

169   A sky classification model is developed using a machine learning method, the k-
170   nearest neighbor (k-NN) algorithm(Cunningham & Delany, 2020). The 8-min AERI-01 and
171   AERI-C1 data between March 1, 2011 to July 31, 2012 are used to train the k-NN model. We
172   use the same inputs and truth data from Raman Lidar as in Turner and Gero (2011). The k-
173   NN classification achieves an accuracy of 94.8%. This algorithm determines the sky to be
174   *clear* or *cloudy*, while the cloudy sky is then further classified to be *thin-cloud* when the 70-
175   minute averaged 985 cm^{-1} brightness temperature is lower than 250K; otherwise, it is
176   classified to be *thick-cloud*. We also tried a classical backpropagation gradient-descent
177   classification algorithm as used by Turner and Gero (2011), which achieves an accuracy of
178   90%. The resulting trends are not sensitive to the classification method chosen. The results
179   presented below are based on the k-NN algorithm.

180   Based on the classification of the *thin-cloud* and *thick-cloud*, the *thick-cloud* emitting
181   temperature range is smaller than that for *thin-cloud* and *clear-sky*, primarily because *thick-
182   clouds* are opaque clouds relatively close to the surface while *thin-cloud* may be either
183   partially cloudy scenes or clouds higher in the troposphere. This is why the *thick-cloud*
184   classification has the smallest standard deviation of DLR among all three different sky
185   conditions.

186   2.3 Homogenization

187   During the overlapping observational period, discrepancies larger than the
188   documented AERI absolute calibration uncertainty (Knuteson et al., 2004a) were noticed
189   between the monthly mean spectra observed by AERI-01 and AERI-C1. Large radiance
190   discrepancies occur especially in the window band and are found to mainly come from clear-
191   sky scenes (see Figure B1 and discussions in Appendix B). This suggests that the
192   discrepancies likely result from calibration(Rowe, Neshyba, Cox, et al., 2011; Rowe,
193   Neshyba, & Walden, 2011) and other undetected errors. In order to avoid discarding
194   meaningful data in the trend analysis, we simulate the clear-sky DLR spectra using a
195   radiation model from the collocated atmospheric measurements and use the synthetic spectra
196   as a reference to assign proper weights in combining the data of AERI-01 and AERI-C1,
197   based on the findings of previous radiance closure studies (e.g., Turner et al., 2004) that
198   demonstrated high accuracy in such synthetic spectra.

199   The radiation model used here is the Line-by-Line Radiative Transfer Model
200   (LBLRTM v12.9) (Clough et al., 2005). To synthesize the clear sky DLR spectra at SGP, we
201   use the temperature and water vapor profiles from the ARM Balloon-Borne Sounding System
202   (https://www.arm.gov/capabilities/instruments/sonde). The water vapor mixing ratio profiles
203   derived from radiosonde are scaled with a height-independent factor to match the precipitable
204   water vapor determined by the microwave radiometer at SGP site. This approach has been
205   used to compensate the dry-bias issue found in the radiosonde water vapor data (Holdridge,
206   2020; Revercomb et al., 2003; Turner et al., 2003; Wang et al., 2002). CO_2 and CH_4
207   concentration profiles are obtained from the CarbonTracker website
208   (http://carbontracker.noaa.gov, Jacobson et al., 2020; Peters et al., 2007). O_3 concentration
209   profiles are adjusted from NASA's Modern-Era Retrospective analysis for Research and
210   Applications, Version 2 (MERRA-2, Gelaro et al., 2017) ozone product to get a better
211   radiative closure with AERI observed DLR (see more details in Appendix B). We use a 200-
212   level input profile for the LBLRTM simulations. The first and second levels are at 0m and
213   10m above ground level respectively. The depth of each subsequent layer is increased by 2%
214   relative to the previous one.

215   As radiosonde observations of near-surface layers are essential to the DLR spectra,
216 the AERI data are selected to match the radiosonde launch time. We keep the spectra whose
217 observation time is within 10 minutes of the radiosonde launch time. For each month, about
218 70 clear sky downwelling longwave spectra are simulated on average. The absolute radiance
219 biases (R_{bias}) are determined as the monthly mean radiance differences between the synthetic
220 and observed DLR spectra.

221   During the overlapping observational period, the monthly mean DLR is combined
222 from AERI-01 and AERI-C1 observed DLR according to Equation (1) and Equation (2) by
223 assigning a ratio r, which represents the proximity of the AERIs observed DLR spectra to the
224 synthetic DLR spectra. In Equation (2), $R_{AERI-01}$ and $R_{AERI-C1}$ represent the observed AERI-
225 01 and AERI-C1 monthly mean DLR respectively.

226
$$r = \frac{R_{bias(AERI-01-LBLRTM)}}{R_{bias(AERI-C1-LBLRTM)}} \tag{1}$$

227
$$R = R_{AERI-01} \times \frac{1}{1+r} + R_{AERI-C1} \times \frac{r}{1+r} \tag{2}$$

228   2.4 Trend detection

229   A weighted linear regression method is applied to detecting the DLR radiance trends.
230 We develop our weighted linear regression model based on the regression model developed
231 by Tiao et al. (1990) and Weatherhead et al. (1998).

232   This model determines the radiance trend, $\hat{\omega}$, in each AERI channel as:

233
$$\hat{\omega} = \frac{\sum_{t=1}^{T} W_t(t-\bar{t})y_t^{\star}}{\frac{1-\phi}{12} \sum_{t=1}^{T} W_t(t-\bar{t})^2} \tag{3}$$

234   In Equation (3), T represents the total number of months. ϕ is the autocorrelation in
235 the noise of the time series considering a first-order autoregressive (AR1) process, and $y_t^{\star}$
236 represents the transformed radiance anomalies (see Figure A1) after removing the effect of
237 the AR1 process (see details in Appendix A). W_t represents the weights which is determined
238 as the intra-month variability of the all-sky observed DLR, shown in Equation (4):

239
$$W_t = \frac{N_t}{\sigma_t^2} \tag{4}$$

240 where N_t and σ_t^2 represent the number and variance of hourly observations in each month.
241 Large variability of DLR radiance results in smaller weights. We use the same weights for all
242 sky types.

243   Along with the magnitude of the trend it is also important to determine the associated
244 uncertainty, $\sigma_{\hat{\omega}}$, which is shown in Equation (5). Here, we mainly account for two sources of
245 uncertainty. First, there is the uncertainty arising from the internal climate variability. This is
246 measured by the term in Equation (5) associated with σ_N and ϕ. Second, there is the
247 uncertainty arising from instrumentation errors measured by the term in Equation (5)
248 associated with σ_e. We assume that two sources of uncertainty are independent of each other.
249 The derivation of Equation (5) is given in Appendix A.

250
$$\sigma_{\hat{\omega}} = \frac{12\sqrt{\sum_{t=1}^{T} W_t^2(t-\bar{t})^2}}{\sum_{t=1}^{T} W_t(t-\bar{t})^2} \sqrt{\sigma_N^2 \frac{1+\phi}{1-\phi} + \sigma_e^2} \tag{5}$$

251   The derived $\sigma_{\hat{\omega}}$ in Equation (5) is referred to as the standard error of the trend
252 magnitude. It is used to test whether the trends deviate significantly from 0 at the 95%
253 significance level. A trend is considered to be significant at the 95% significance level if the
254 trend magnitude is roughly larger than $2\sigma_{\hat{\omega}}$. In following figures, the uncertainty envelope
255 corresponds to the 95% confidence interval.

256   **3 Results**

257   3.1 All-sky radiance trends

258   The homogenized downwelling longwave radiance records have been constructed,
259 based on monthly averaged AERI-01 data from 1996 to 2013 and AERI-C1 data from 2004
260 to 2018. In total, we have 23 years of DLR data at SGP for analysis.

261   It can be inferred from the monthly anomalies shown in Figure 4 that the DLR
262 radiance trends depend on the analysis period as the anomalies do not show monotonic
263 changes over this 23-year period. It is noticeable that AERI-01 data (Figure 4a) show
264 decreasing trends in window-band (800-1200 cm^{-1}) DLR, which is consistent with the
265 negative trends detected in Gero and Turner (2011). Including AERI-C1 data (Figure 4b)
266 affords a longer DLR spectral record; the latest few years are especially characterized by
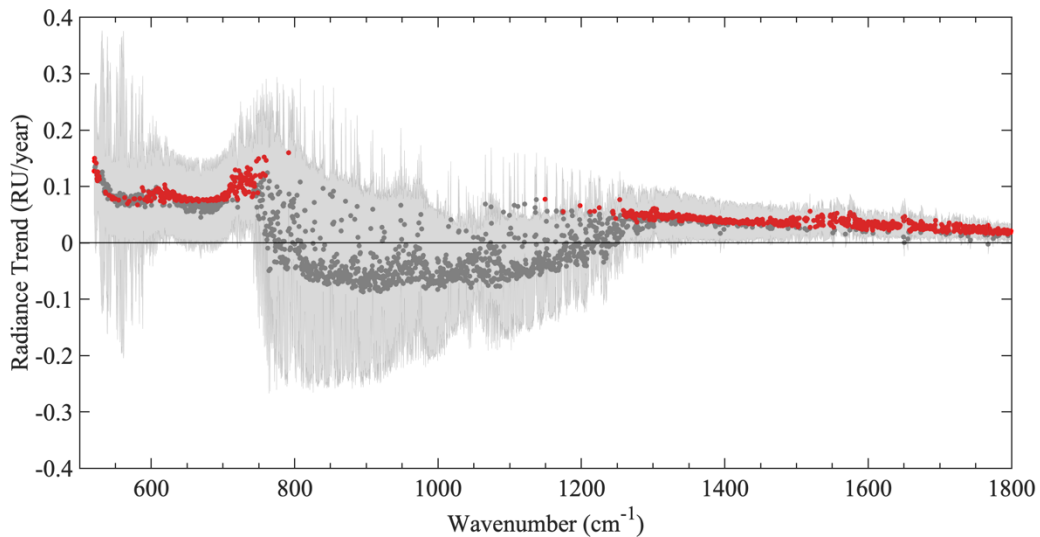267 warm anomalies.

268

269   **Figure 5.** The all-sky radiance trends. Each dot represents the trend at a different AERI
270 channel and the trends in reds pass the 95% significance test while the grey ones do not. The
271 shading in the figure is the 95% confidence interval.

272   The long-term all-sky radiance trends over the period of 1996-2018 are shown in
273 Figure 5. The all-sky DLR trends have different features in different spectral bands. In the
274 CO$_2$ absorption band centered around 667 cm^{-1}, the trends are generally positive (increasing)
275 and are statistically significant in the wings but not at the center. In the window band (800-
276 1200 cm^{-1}), there are no statistically significant trends. In the water vapor absorption band
277 (1300-1800 cm^{-1}), similar to the CO$_2$ absorption band, the radiance trends are generally
278 positive and statically significant.

279   DLR radiance in different AERI channels are controlled by different meteorological
280 variables. To illustrate this point, Figure 6a shows the correlation coefficients between the
281 deseasonalized and detrended monthly anomalies in the radiance (brightness temperature)

282   spectra from the two AERIs and surface air temperature from ERA5. Note that AERI-01 and
283   AERI-C1 have different observational periods, which can cause the correlation coefficients
284   difference between AERI-01 and AERI-C1 especially in the window band. In the center of
285   the CO_2 absorption band (667 cm^{-1}) and channels corresponding to strong H_2O absorption
286   lines, the correlation coefficient is close to one, indicating that the variance in the radiance in
287   these channels is primarily controlled by the surface air temperature. This is because the
288   atmospheric absorption is strongly saturated in these channels and thus they are less sensitive
289   to variations in the concentrations of the gases themselves. In comparison, at the wings of the
290   CO_2 band and the weaker H_2O absorption lines, the atmospheric absorption is not saturated
291   so that variability in DLR radiance is subject to the variation in the temperature and gas
292   concentration, meaning that the trends both in temperature and gas concentrations drive the
293   radiance to increase, which explains the stronger and statistically more significant trend
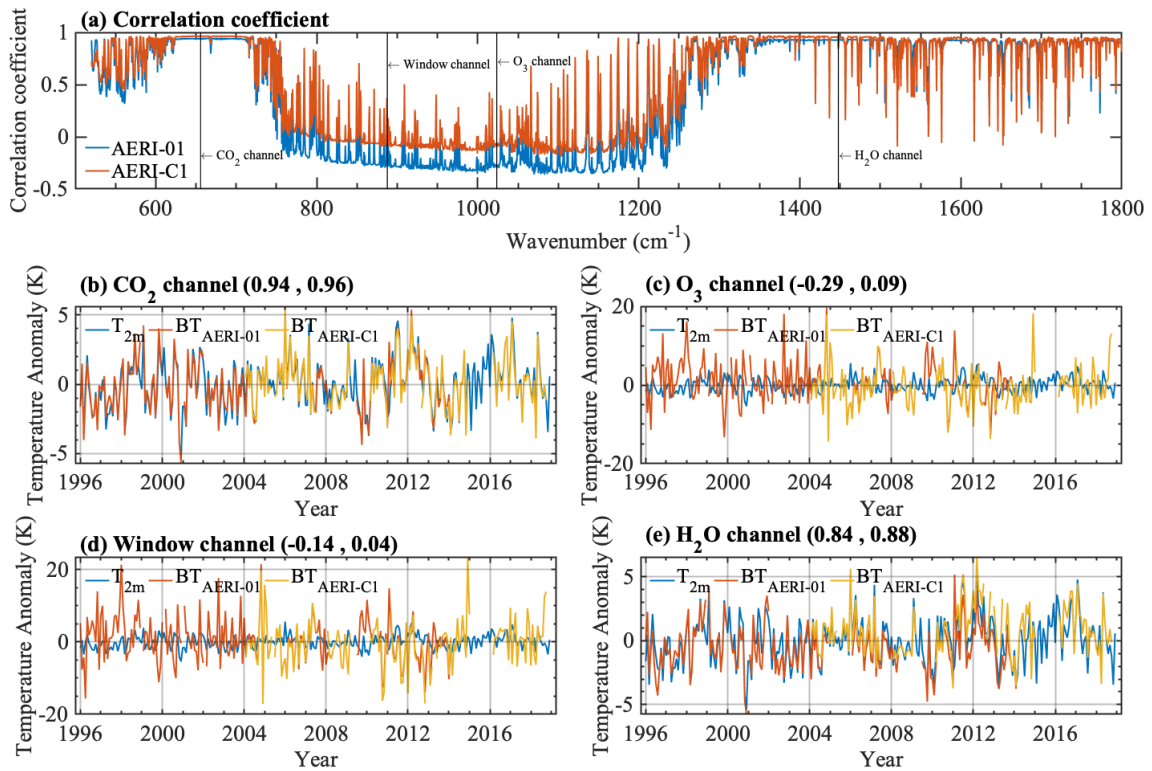294   signals in these channels, as seen in Figure 5.

295

Figure 6. (a)The correlation coefficient between the AERI observed brightness temperature
spectra and near surface air temperature from ERA5. (b-e) The time series of the
deseasonalized brightness temperature and near surface air temperature in four AERI
channels. In each title, the values in the brackets are the correlation coefficients between near
surface air temperature from ERA5 and observed brightness temperature by AERI-01 and
AERI-C1 respectively.

302   In Figure 6, the time series of the brightness temperature in four selected AERI
303   channels: a CO_2 channel at 655.72 cm^{-1}, a window channel at 887.63 cm^{-1}, a O_3 channel at
304   1023.60 cm^{-1}, and a H_2O channel at 1447.89 cm^{-1} (Figure 6b to 6e) are displayed. There is
305   good consistency between the AERI-01 and AERI-C1 observed brightness temperature in all
306   four channels. The all-sky brightness temperature at the CO_2 channel follows closely with the
307   surface air temperature from ERA5 (Figure 6b). The near-surface warming of 0.045 K/year
308   (Figure 1) is equivalent to 0.071 RU/year at this channel, which is close to the observed all-
309   sky radiance trend of ~0.072 RU/year (averaged trend between nearby 5 channels). In the
310   H_2O channel, the brightness temperature measured by the AERIs also follows the near

311 surface air temperature (Figure 6e) but not as close as the CO_2 channel (Figure 6b). In
312 contrast, the brightness temperature anomalies in the window and O_3 channels have larger
313 fluctuations than that at the CO_2 and H_2O channels and are evidently decoupled from the near
314 surface air temperature (Figure 6c and 6d).

315 That the radiance trend is reinforced by the warming and opacity effects in the weak
316 absorption channels leads to benefits of using these AERI measurements in climate change
317 detection. Assuming the trend magnitude and uncertainty determined from the 23-year
318 records hold unchanged into future, the years to detect a significant trend, $n^\star$, at 90%
319 significance level is:

$$320 \qquad n^\star \approx \frac{3.3\sigma_{\widehat{\omega}}}{|\widehat{\omega}|} \times 23 \; years \qquad\qquad (6)$$

321 where $\widehat{\omega}$ is the 23-year trend determined by Equation (3) and $\sigma_{\widehat{\omega}}$ is the trend
322 uncertainty determined by Equation (5). Based on this equation, approximately 30 years are
323 needed to detect a significant trend in the 2-meter air temperature from the ERA5 data shown
324 in Figure 1. In comparison, Figure 7 shows earlier detectability of the radiance trends in weak
325 absorption channels, such as in the wings of the CO_2 band and in the weak absorption
326 channels in the H_2O vibration-rotational band. We can conclude that it is advantageous to
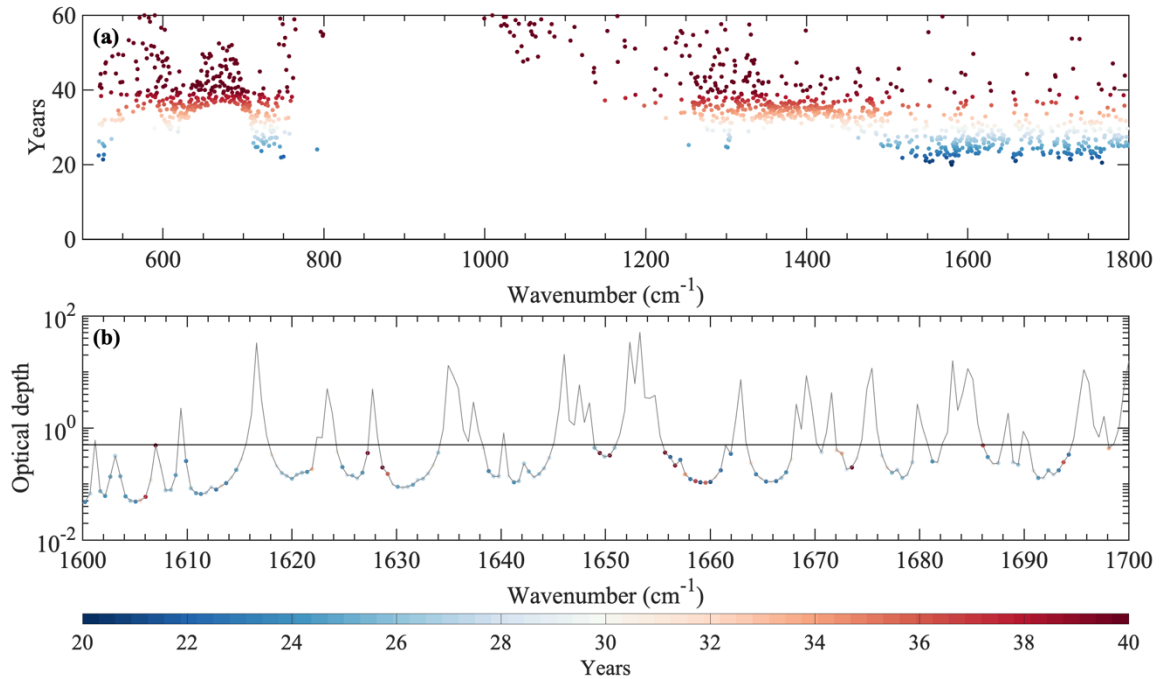327 monitor the DLR radiance in these channels for climate change detection.

328
329 **Figure 7.** Trend detectability. (a) Time to detect (T2D) radiance trends at 90% significance
330 level in different AERI channels; in comparison, the T2D for the 2-meter temperature from
331 the ERA5 reanalysis is about 30 years. (b) The T2D (color-coded), in relation to atmospheric
332 absorption strength, measured by the optical depth of a 1-meter-thick atmospheric layer near
333 the surface. The horizontal line marks optical depth of 0.5.

334 Trend detection in the radiance record is determined by comparing the trend signal to
335 the uncertainties arising from different causes. Here, based on Equation (5), we account for
336 uncertainties arising from climate internal variability (σ_N) and also instrumentation error (σ_e)
337 (Figure 5). The overall uncertainty is notably large in the window band for the all-sky
338 condition (Figure 5) or for different sky conditions (Figure 9), which impedes the detection of

339 any significant radiance trends in this especially variable spectral band. The analysis of the
340 respective parameters in Appendix A (see Figure A2) indicates the climate internal variability
341 dominates the instrumentation error when shaping the overall uncertainty envelope in Figure
342 5. It is found that the influence of the autoregressive process also does not strongly influence
343 the trend uncertainty, as evident by the small value of ϕ, especially in the window band. We
344 conclude that the trend uncertainty mainly arises from the internal climate variability.

345   3.2 Trends in different cloud conditions

346   The results presented in the previous subsection demonstrate that the radiance trends
347 in the window band are different from the greenhouse gas absorption bands; the window
348 band also is prone to high levels of uncertainty due to the marked variability of the signal that
349 ranges from small values in clear sky conditions to large values when opaque low-altitude
350 clouds are overhead. Given the fact that clouds are a significant factor that influences this
351 band (see Figure 2), we analyze the radiance trends under different cloud conditions in this
352 subsection.

353   The fraction of time that each sky conditions occur in one month (referred as 'sky
354 fractions') based on the hourly spectra are shown in Figure 8. First, there is a good agreement
355 between AERI-01 and AERI-C1 in the sky fraction monthly time series, with correlation
356 coefficients of 0.94, 0.89, and 0.94 for clear-sky, thin cloudy-sky, and thick cloudy-sky,
357 respectively. The clear-sky fraction between June 1996 and May 2010 from our classification
358 is around 42% which is comparable to what was found by Turner and Gero (2011).

359   The clear-sky fraction increases at a rate of 0.17±0.09 % per year, while the thick
360 cloudy-sky fraction decreases at a rate of -0.18±0.09 % per year. There is no significant trend
361 for thin cloudy-sky fraction. The reason why the sky fraction trends for different sky
362 conditions are different warrant further investigation in future work.
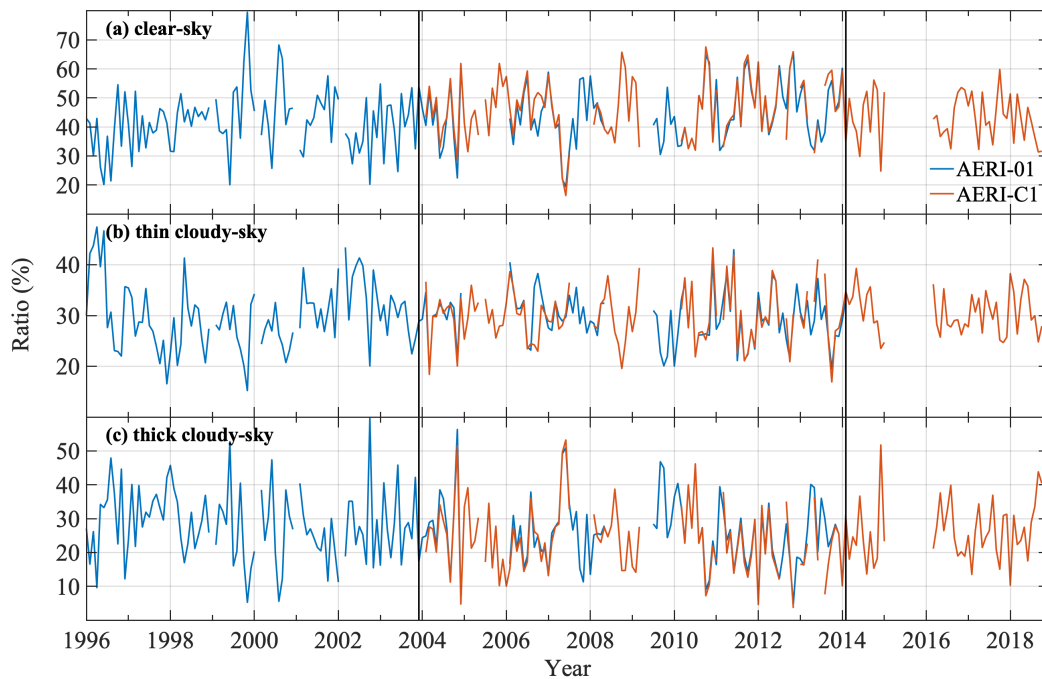

363

Figure 8. The monthly sky fractions of different sky conditions, categorized based on 8-
minute mean spectra at SGP site. The overlapping observational period is between the two
vertical thick black lines.

367   Trends in DLR radiance for different sky types based on the k-NN classifier are
368   shown in Figure 9. In the window band, the clear-sky and thin cloudy-sky trends are positive,
369   while the thick cloudy-sky trends are negative; however, none of those trends is statistically
370   significant from zero. In the spectral regions outside the window band, the trends for different
371   sky types are generally positive and have the same features as the all-sky scene.
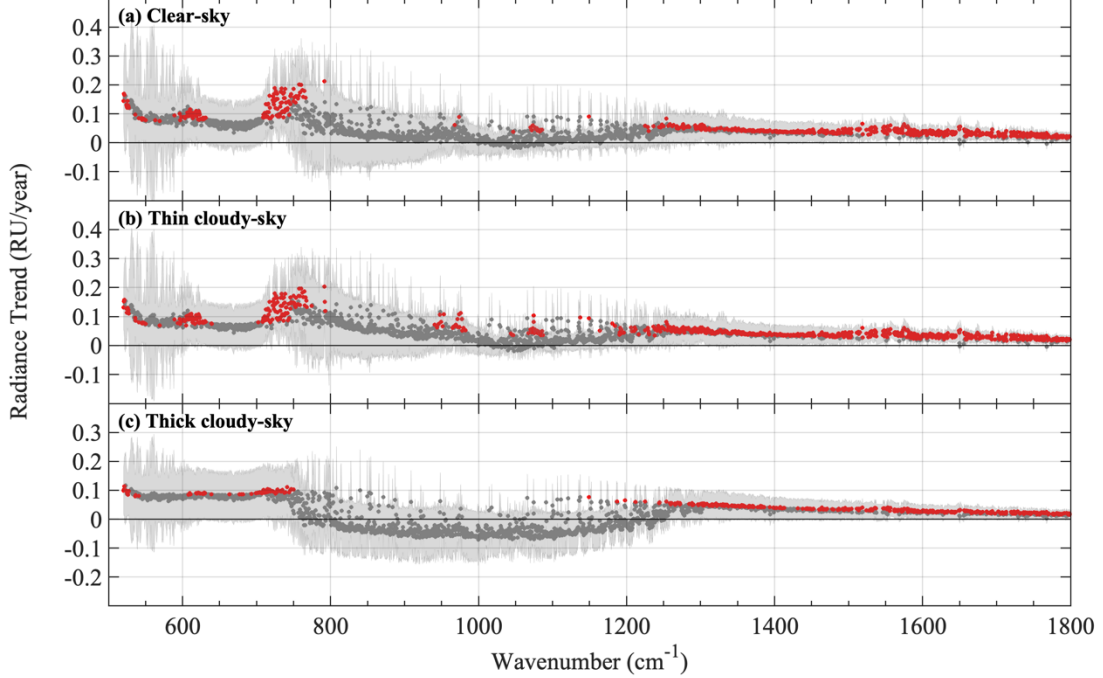

372

Figure 9. The trends in DLR radiance for different sky types at SGP site. Each dot represents
the trend at a different AERI channel and the trends in red pass the 95% significance test
while the grey ones do not. The shading in the figure is the 95% confidence interval.

376   The all-sky DLR trends is caused by changes in both sky fraction and radiance of
377   each sky type. We use equation (7) to separate the contributions from these factors, in which
378   R_{all} represents the all-sky radiance, f_i and R_i represent the sky fraction and mean radiance
379   for different sky types.

$$\frac{dR_{all}}{dt} = \sum \frac{df_i}{dt} R_i + \sum \frac{dR_i}{dt} f_i + residual \qquad (7)$$

381   The results of decomposed trends based on Equation (7) are shown in Figure 10. The
382   small residual term (purple line in Figure 10a), which comes from the nonlinear effects,
383   suggests that the overall all-sky radiance trends can be well explained by Equation (7). In the
384   window band, the overall radiance trends are a result of the compensation between the sky
385   fraction change (orange line in Figure 10a) and the radiance change (yellow line in Figure
386   10a). While in the CO_2 absorption band (centered at 677 cm^{-1}) and H_2O absorption band
387   (1300 − 1800 cm^{-1}), the overall radiance trends are caused by radiance change which is due
388   almost entirely to the increases in the near-surface temperature because the atmosphere is
389   already too opaque to reflect any gas concentration changes.

390   The overall radiance trends caused by sky fraction changes (orange line in Figure 10a)
391   are a result of the compensation between changes in the clear-sky (blue line in Figure 10b)
392   and the thick cloudy-sky fraction (yellow line in Figure 10b). In the CO_2 absorption band
393   (centered at 677 cm^{-1}) and H_2O absorption band (1300 − 1800 cm^{-1}), there is a perfect

394   compensation resulting in almost no trends. In the window band, the negative trends are
395   mainly caused by the thick cloudy-sky fraction change.

396   In the window band (800 -1200 cm^{-1}), the overall radiance trends caused by radiance
397   change (yellow line in Figure 10a) result from the compensation between positive clear-sky
398   and thin cloudy-sky radiance change trends and negative thick-cloudy sky radiance change
399   trends. While in the CO_2 absorption band (centered at 677 cm^{-1}) and H_2O absorption band
400   (1300 – 1800 cm^{-1}), the radiance changes for the three sky types all contribute similarly to the
401   overall radiance trends caused by radiance change.
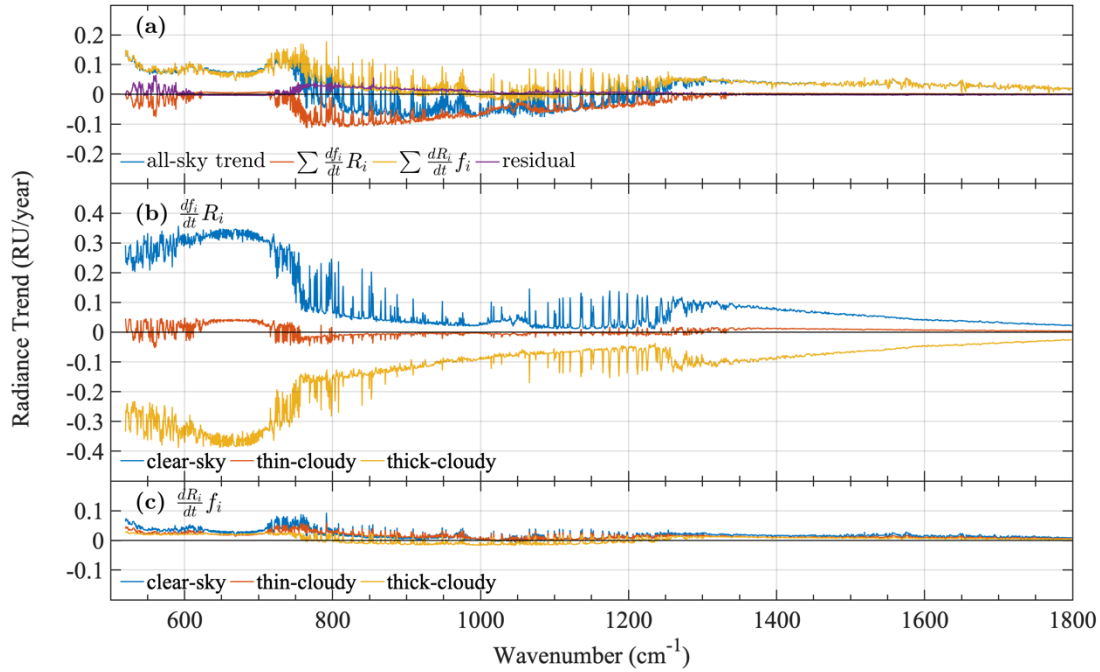

402

403   **Figure 10.** The all-sky DLR trends decomposed to the contributions from the sky fraction
404   and radiance changes of different sky types. (a) The blue line represents the calculated all-
405   sky DLR trends which is the same as that from Figure 5. Orange and yellow lines represent
406   the contribution from sky fraction change and radiance change determined using equation (7)
407   respectively. The purple line is the residual term from Equation (7); (b) The all-sky DLR
408   trends caused by sky fraction change. The blue, orange, and yellow lines represent the
409   contributions from clear-sky, thin cloudy-sky, and thick cloudy-sky fraction changes
410   respectively; (c)The all-sky DLR trends caused by radiance change. The blue, orange, and
411   yellow lines represent the contributions from clear-sky, thin cloudy-sky, and thick cloudy-sky
412   radiance changes respectively.

4 Discussion and Conclusions

414   In this study, a long-term record of DLR at SGP site have been constructed for
415   analyzing the DLR trends, based on a weighted linear regression method which considers
416   both natural climate variability and measurement error. Compared to previous studies, our
417   analysis is based on a longer DLR record combined from the two AERIs at the SGP site and
418   makes use of synthetic DLR data in validating and differentiating the AERI measurements
419   over their overlapping observational period. In addition, we quantitatively decompose the
420   overall radiance trends due to the contributions from sky fraction change and radiance
421   change.

422   The trends in DLR in different spectral ranges have different features. The trends are
423 generally positive in the CO_2 and H_2O absorption bands, while no statistically significant
424 trends are detected in the window band (Figure 5). We find that in the centers of the CO_2 and
425 H_2O absorption bands, the radiance are controlled by the near-surface air temperature (Figure
426 6) because of the strong saturated atmospheric absorption. The sensitivity of DLR to near-
427 surface air temperature indicates the potential of DLR to monitor climate change. In the
428 wings of these absorption bands, both the near surface atmospheric warming and the increase
429 of the abundance of these trace gases contribute to the radiance trends (Feldman et al., 2015),
430 which makes climate trend signal more readily detectable, as hypothesized by Huang (2013).
431 In the window band, the radiance are decoupled from the near surface air temperature (Figure
432 6) because of the impact of sky-fraction changes of different scenes (clear and cloudy-skies).

433   We find that the sky fraction change and the radiance change led to compensating
434 effects on the DLR trends. This compensation results in weakly (statistically insignificant)
435 negative radiance trends in the window band (Figure 10). In contrast, the radiance trends are
436 dominated by the radiance change in the CO_2 and H_2O absorption bands, which are similar in
437 all three sky types.

438   The influences of both climate natural variability and measurement error are
439 considered when determining the uncertainty of the trend magnitude (Equation (5), Figure
440 A2). We find that for all the sky types, the majority of the uncertainty comes from the natural
441 variability. This underlines the necessity of continuous DLR measurements to ascertain the
442 DLR trends, especially in the mid-infrared window (Figure 5).

443   The two AERIs at the SGP site provide us an excellent opportunity to test the
444 accuracy and consistency of the instruments. The discrepancies between the two AERIs in
445 the overlapping periods may have come from calibration error and other undetected
446 instrumentation errors. In this study, we use synthetic data to differentiate and combine the
447 two AERIs' observations. Further investigation is required to understand the origin of the
448 discrepancies and therefore to assure the measurement accuracy.

449   This paper has focused on the detection, as opposed to attribution, of the DLR trends.
450 In the clear-sky case, atmospheric temperature and radiative gas concentration changes
451 (primarily in water vapor) are likely the main contributors to the DLR radiance changes. As
452 for the cloudy-sky case, changes in both the atmospheric states and cloud properties may
453 contribute to the DLR radiance changes. Future work is warranted to understand and
454 quantitatively attribute the DLR trends disclosed in this paper to different meteorological
455 variables.
456
468
469

470 **Appendix A: Trend Detection**

471   We first summarize the linear trend model and trend estimation from Tiao et al.
472 (1990) and Weatherhead et al. (1998) in A.1 and A.2. We adopt the same notation in their
473 papers. Then we add the measurement error term to the trend detection in A.3 following Tiao
474 et al. (1990).

475   A.1 Basic linear trend modeling

476   In order to detect the linear trend, we first construct a simple model that describes the
477 monthly mean radiance Y_t as:

$$Y_t = \mu + S_t + \omega X_t + N_t, t = 1, \cdots, T \tag{A1}$$

479 where μ is a constant term, S_t represents the seasonal component, ω is the trend magnitude to
480 be determined, $X_t = \frac{t}{12}$ represents time measured in the units of year, N_t represents the
481 unexplained portion of the data, i.e. the noise, and T represents the length of data set in
482 months.

483   The seasonal component S_t is determined by taking long-term average of each
484 calendar month. This component is subsequently removed from the monthly mean.

$$y_t = Y_t - S_t = \mu + \omega X_t + N_t, t = 1, \cdots, T \tag{A2}$$

486   The noise N_t is assumed to be autoregressive of the order of 1 (AR1):

$$N_t = \phi N_{t-1} + \epsilon_t \tag{A3}$$

488 where ϵ_t are the random white noise with zero mean and common variance σ_ϵ^2,
489 $\epsilon_t \sim W(0, \sigma_\epsilon^2)$. The autocorrelations in the noise come from various natural factors. ϕ is
490 determined as the autocorrelation coefficient of the AR1 process after removing from y_t a
491 linear trend component obtained by regressing y_t to time using a simple weighted linear least
492 squares method (i.e., neglecting the AR1). The all-sky ϕ is shown in Figure A2a.

493   The variance of the noise N_t can also be determined from the detrended y_t time
494 series:

$$\begin{aligned} \sigma_N{}^2 \quad &= Cov(N_t, N_t) = Cov(\phi N_{t-1} + \epsilon_t, \phi N_{t-1} + \epsilon_t) \\ &= \phi^2 Cov(N_{t-1}, N_{t-1}) + Cov(\epsilon_t, \epsilon_t) \\ &= \phi^2 \sigma_N{}^2 + \sigma_\epsilon{}^2 \end{aligned} \tag{A4}$$

496   Thus,

$$\sigma_N{}^2 = \frac{\sigma_\epsilon{}^2}{1 - \phi^2} \tag{A5}$$

498   A.2 Trend estimation with weights

499   Given ϕ, to obtain the trend estimation, we consider a transformed model:

$$\begin{aligned} y_t{}^\star \quad &= y_t - \phi y_{t-1} \\ &= \mu(1 - \phi) + \omega(X_t - \phi X_{t-1}) + \epsilon_t \\ &= \mu(1 - \phi) + \omega \left[\frac{t - \phi(t-1)}{12} \right] + \epsilon_t \\ &= \mu(1 - \phi) + \frac{\omega\phi}{12} + \frac{\omega(1 - \phi)t}{12} + \epsilon_t \\ &= \mu^\star + \omega t^\star + \epsilon_t \end{aligned} \tag{A6}$$

501   where $\mu^\star = \mu(1-\phi) + \frac{\omega\phi}{12}$ and $t^\star = \frac{(1-\phi)t}{12}$. Thus, in the transformed model, there is no
502   more noise term N_t.

503   The transformed DLR radiance $y_t{}^\star$ is shown in Figure A1.

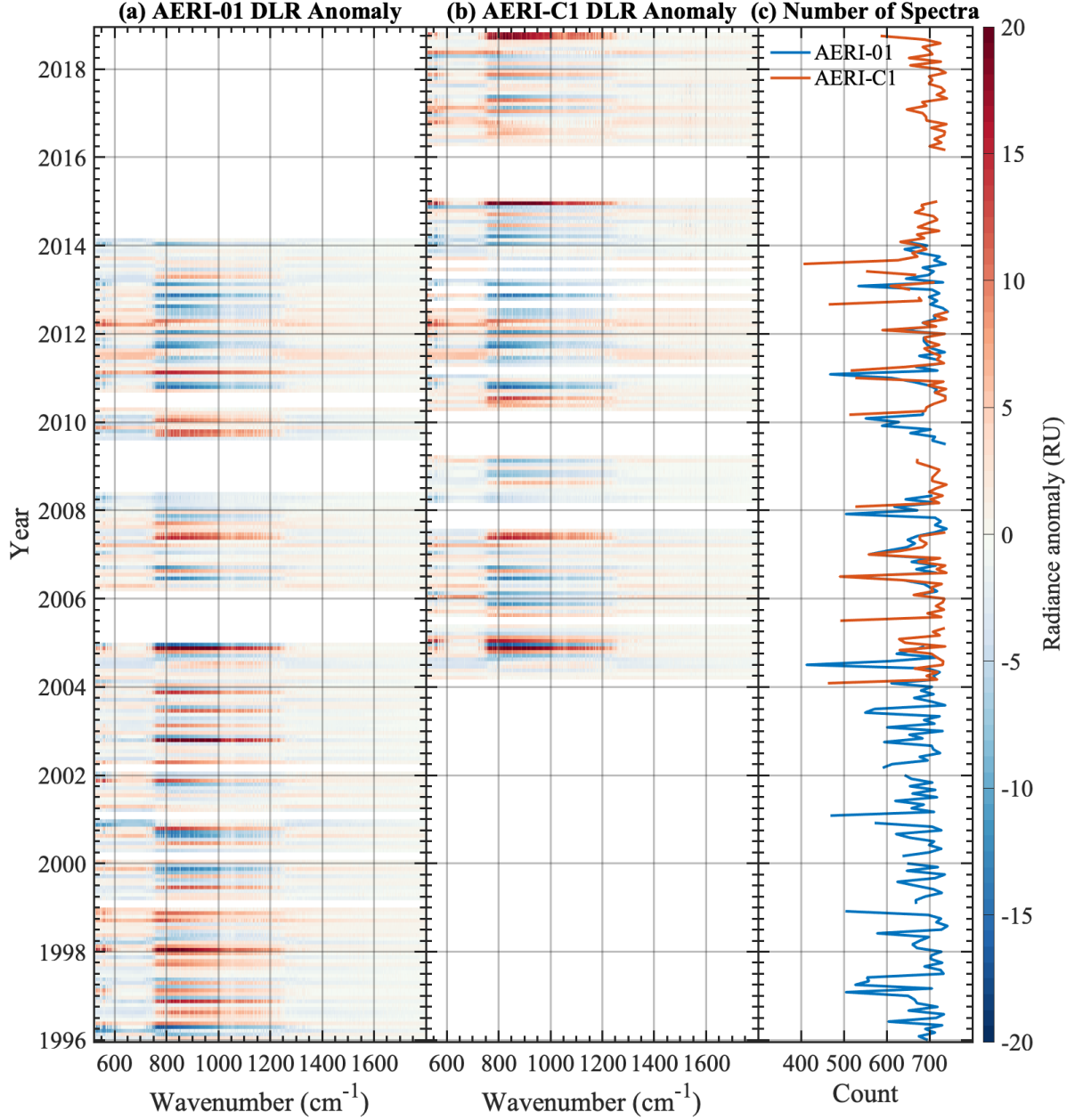**Figure A1.** Transformed monthly anomaly of AERI-observed radiance based on Equation (A6).

507   According to the weighted least square estimation:

508
$$\widehat{\omega} = \frac{\sum_{t=1}^{T} W_t(t^\star - \overline{t^\star})y_t{}^\star}{\sum_{t=1}^{T} W_t(t^\star - \overline{t^\star})^2} = \frac{\sum_{t=1}^{T} W_t(t - \overline{t})y_t{}^\star}{\frac{1-\phi}{12}\sum_{t=1}^{T} W_t(t - \overline{t})^2} \tag{A7}$$

509   where W_t represents the weights determined according to Equation (4), $\overline{y_t^{\star}} = \frac{\sum_{t=1}^{T} W_t y_t^{\star}}{\sum_{t=1}^{T} W_t}$, $\overline{t^{\star}} =$

510     $\frac{\sum_{t=1}^{T} W_t t^{\star}}{\sum_{t=1}^{T} W_t}$, and $\overline{t} = \frac{\sum_{t=1}^{T} W_t t}{\sum_{t=1}^{T} W_t}$.

511   The variance of the estimated ω:

512
$$\sigma_{\hat{\omega}}^2 = Var(\hat{\omega}) = Var\left[\frac{\sum_{t=1}^{T} W_t(t-\overline{t})y_t^{\star}}{\frac{1-\phi}{12}\sum_{t=1}^{T} W_t(t-\overline{t})^2}\right] = \frac{Var\left[\sum_{t=1}^{T} W_t(t-\overline{t})y_t^{\star}\right]}{(\frac{1-\phi}{12})^2\left[\sum_{t=1}^{T} W_t(t-\overline{t})^2\right]^2}$$

513
$$= \frac{Var\left[\sum_{t=1}^{T} W_t(t-\overline{t})\epsilon_t\right]}{(\frac{1-\phi}{12})^2\left[\sum_{t=1}^{T} W_t(t-\overline{t})^2\right]^2} = \frac{\sum_{t=1}^{T}[Var[W_t(t-\overline{t})\epsilon_t]]}{(\frac{1-\phi}{12})^2\left[\sum_{t=1}^{T} W_t(t-\overline{t})^2\right]^2}$$

514
$$= \frac{Var(\epsilon_t)\sum_{t=1}^{T} W_t^2(t-\overline{t})^2}{(\frac{1-\phi}{12})^2\left[\sum_{t=1}^{T} W_t(t-\overline{t})^2\right]^2} = \frac{\sigma_{\epsilon}^2\sum_{t=1}^{T} W_t^2(t-\overline{t})^2}{(\frac{1-\phi}{12})^2\left[\sum_{t=1}^{T} W_t(t-\overline{t})^2\right]^2} \quad (A8)$$

515
$$\sigma_{\hat{\omega}} = \frac{\sigma_{\epsilon}}{\frac{1-\phi}{12}}\frac{\sqrt{\sum_{t=1}^{T} W_t^2(t-\overline{t})^2}}{\sum_{t=1}^{T} W_t(t-\overline{t})^2} = \sigma_N g(T,\phi,W) \quad (A9)$$

516
$$g(T,\phi,W) = \sqrt{\frac{1+\phi}{1-\phi}}\frac{12\sqrt{\sum_{t=1}^{T} W_t^2(t-\overline{t})^2}}{\sum_{t=1}^{T} W_t(t-\overline{t})^2} \quad (A10)$$

517   Thus,

518
$$\sigma_{\hat{\omega}} = \sigma_N\sqrt{\frac{1+\phi}{1-\phi}}\frac{12\sqrt{\sum_{t=1}^{T} W_t^2(t-\overline{t})^2}}{\sum_{t=1}^{T} W_t(t-\overline{t})^2} \quad (A11)$$

519   From equation (A11), we conclude that the trend uncertainty is affected by the
520   length of the available data, the natural variability in the data, the autocorrelation of the data
521   and the weights.

522   A.3 Effect of measurement error

523   When we consider the instrumentation errors e_t in the measurements, Equation A2
524   becomes:

525
$$y_t = \mu + \omega X_t + N_t + e_t, t = 1, \cdots, T \quad (A12)$$

526   e_t is considered to be white noise with zero mean and common variance σ_e^2,
527     $e_t \sim W(0,\sigma_e^2)$, and independent of N_t because N_t originates from unobserved or unsuspected
528   atmospheric factors, while e_t comes from the instrument itself.

529   In this case, the variance of noise comes from two parts:

530
$$\sigma^2 = \sigma_N^2 + \sigma_e^2 \quad (A13)$$

531   Similar to the derivation in Equation (A9), the variance of the estimated trend
532   magnitude is:

$$\sigma_{\hat{\omega}}^2 \qquad = \sigma_N^2 g^2(T,\phi,W) + \sigma_e^2 g^2(T,0,W)$$

$$= \sigma_N^2 \frac{1+\phi}{1-\phi} \frac{144 \sum_{t=1}^{T} W_t^2(t-\bar{t})^2}{\left[\sum_{t=1}^{T} W_t(t-\bar{t})^2\right]^2} + \sigma_e^2 \frac{144 \sum_{t=1}^{T} W_t^2(t-\bar{t})^2}{\left[\sum_{t=1}^{T} W_t(t-\bar{t})^2\right]^2} \qquad (A14)$$

$$= \left(\sigma_N^2 \frac{1+\phi}{1-\phi} + \sigma_e^2\right) \frac{144 \sum_{t=1}^{T} W_t^2(t-\bar{t})^2}{\left[\sum_{t=1}^{T} W_t(t-\bar{t})^2\right]^2}$$

The uncertainty of the all-sky radiance trend magnitude caused by the natural variability and the measurement error are shown in Figure A2b.
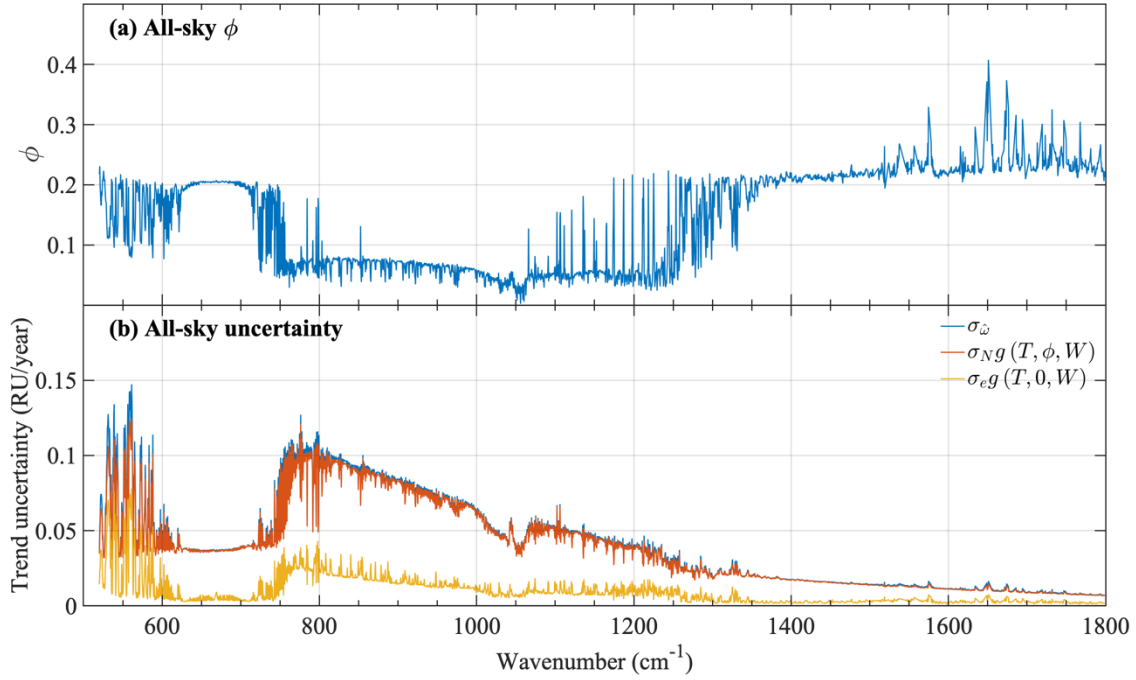

Figure A2. Parameters concerning the radiance trends. (a) The all-sky autocorrelation coefficient considering AR1 process; (b) All-sky DLR trend uncertainty decomposition based on Equation (A14). The blue line represents the total all-sky trend magnitude uncertainty. The orange and yellow lines represent the all-sky trend magnitude uncertainty arising from climate natural variability and measurement error respectively.

A.4 Time to detect the trend

The trend detection ω is judged to be real or significantly different from zero at the 5% level if $|\hat{\omega}| > 2\sigma_{\hat{\omega}}$. $\hat{\omega}$ is approximately normally distributed, so $z = \frac{\hat{\omega}-\omega}{\sigma_{\hat{\omega}}}$ follows a standard normal distribution.

$$Pr(|\hat{\omega}| > 2\sigma_{\hat{\omega}}) = Pr\left(z > 2 - \frac{\omega}{\sigma_{\hat{\omega}}}\right) \qquad (A15)$$

To detect a real trend of specified magnitude $|\omega|$, with probability of 90%: $2 - \frac{\omega}{\sigma_{\hat{\omega}}} < -1.3 \Rightarrow \omega > 3.3\sigma_{\hat{\omega}}$.

Thus, the number of years $n^\star$ of data required to detect the trend $\hat{\omega}$ which is determined based on 23-year data:

551
$$n^{\star} \approx \frac{3.3\sigma_{\widehat{\omega}}}{|\widehat{\omega}|} \times 23 \; years \qquad\qquad (A16)$$

552

553 **Appendix B: Homogenization of the two AERI records**

554   B.1 Comparison between the two AERIs

555   During the overlapping observation period, the all sky monthly mean radiance
556 difference between AERI-01 and AERI-C1 is shown in Figure B1. Since these two
557 instruments have different sampling frequency, the AERI-C1 spectra are averaged to match
558 the sampling of AERI-01 spectra before the comparison. From Figure B1a, there are
559 noticeable discrepancies between the AERI-01 and AERI-C1 observations. Because of the
560 different sampling frequency, the two AERIs have random errors of different amplitudes
561 (Turner et al., 2006). However, we find that removing the random errors using the principal
562 component analysis following Turner et al. (2006) has little impact on the discrepancies (not
563 shown). We find that in more than 20% of the AERI channels in the spectral range from 700
564 to 1300 cm^{-1} and for more than 12% of the overlapping observational months, the radiance
565 difference between two AERIs is larger than the documented absolute calibration uncertainty
566 (Knuteson et al., 2004a).

567   For AERI-C1 data stream, multiple instruments were used. All these transitions can
568 be seen in Figure B1a subtly or obviously. First, the transition from AERI-04 to AERI-05
569 happened in September 2009, which is subtly visible and is labelled by the green star in
570 Figure B1a. Next, in March 2010, the instrument changed from AERI-05 to AERI-06, which
571 is labelled by the green triangle in Figure B1a. Then, the transition from AERI-06 to AERI-
572 106 happened in March 2011, which is very obviously visible and is labelled by the green
573 square in Figure B1a. AERI-106 operated until July 2013 and was being replaced by AERI-
574 108 until present. It's interesting that the radiance differences between all of these "AERI-
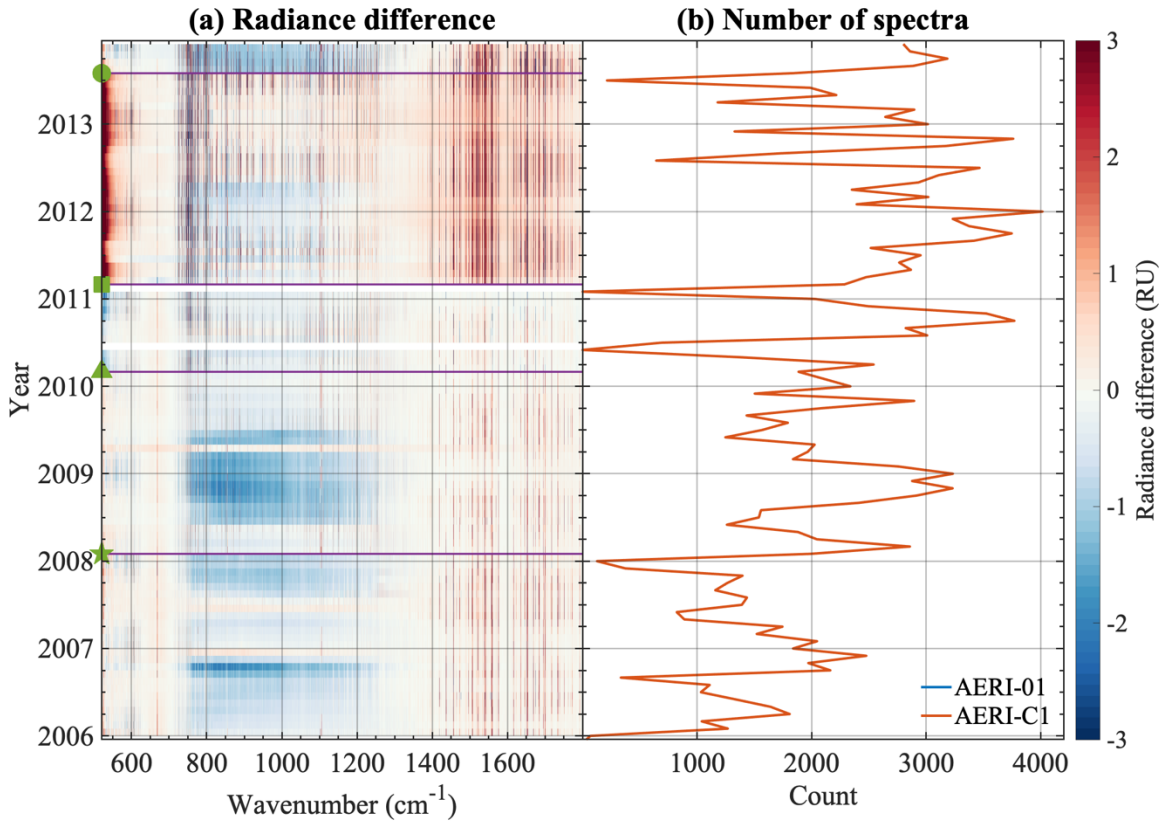575 C1" instruments and the AERI-01 have unique spectral signatures.

Figure B1. (a) The monthly mean DLR difference between AERI-C1 and AERI-01 (AERI-C1 – AERI-01). The green symbols mean the time of AERI-C1 instrument transition; (b) Number of 8-min spectra for each month (the counts are identical after AERI-C1 spectra are resampled to match AERI-01).

When separating the measured spectra to different sky types, we find that the prominent difference between the two AERIs in the window band mainly comes from relatively clear sky conditions. Figure B2 shows the monthly mean radiance difference for different sky types in October 2006 as an example. Here the DLR radiance at 985 cm^{-1} is used to classify the sky to be relatively clear (<40 RU) or relatively cloudy (>40 RU). We chose 40 RU based on the threshold that Turner and Gero (2011) used to classify cloudy sky to be thin or thick clouds scenes.
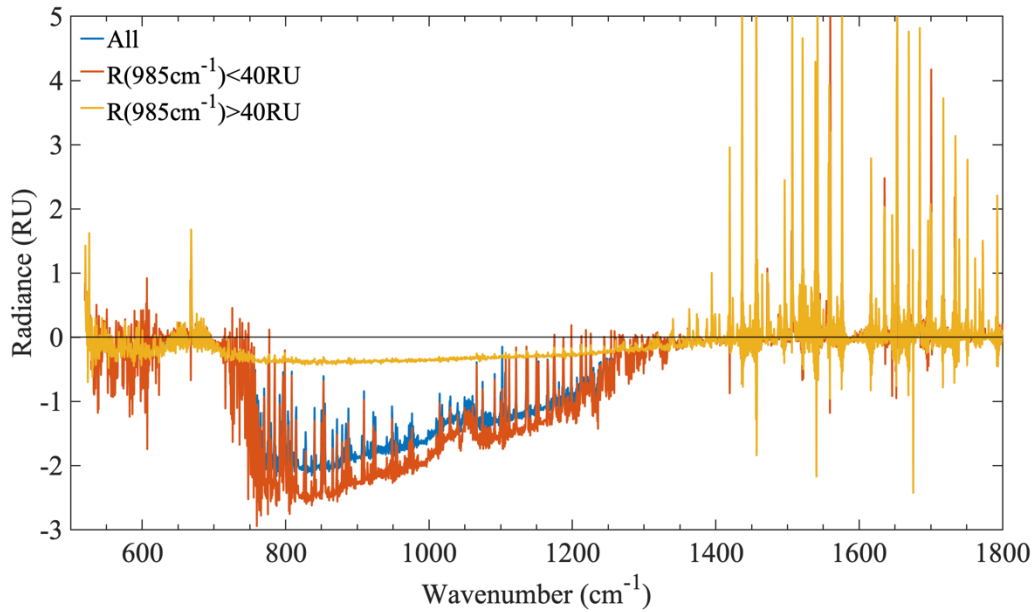
588

Figure B2. The monthly mean DLR difference between AERI-C1 and AERI-01 (AERI-C1 –
AERI-01) for different sky conditions in October 2006

591   We examined various instrumental parameters recorded with AERI measurements,
592 including calibration blackbody temperatures, instrument responsivity, and so on, but found
593 that no instrumental parameter can indicate the radiance difference between the two AERIs.

594   B.2 Clear-sky LBLRTM simulations

595   Since the differences between two AERIs mainly come from relatively clear sky
596 scenes, we use clear sky synthetic spectra simulated from LBLRTM as a metric to distinguish
597 their relative accuracies. Here we use the classical backpropagation gradient-descent
598 classification algorithm mentioned in Subsection 2.2 to select clear-sky spectra. To make sure
599 the sky chosen is clear, we set the algorithm threshold to be 0.8, which means the possibility
600 of the sky to be clear is at least 0.8.

601   After matching all datasets including radiosonde dataset and gas concentrations
602 datasets at SGP mentioned in the Method section to select atmospheric profiles, clear sky
603 synthetic spectra are obtained during the overlapping observational period. For each month,
604 about 70 downwelling longwave spectra are simulated on average. The LBLRTM simulation
605 is validated based on the test in Feldman et al. (2015). We chose the same time slices selected
606 in Feldman et al. (2015) to simulate the DLR spectrum and we can achieve similar radiative
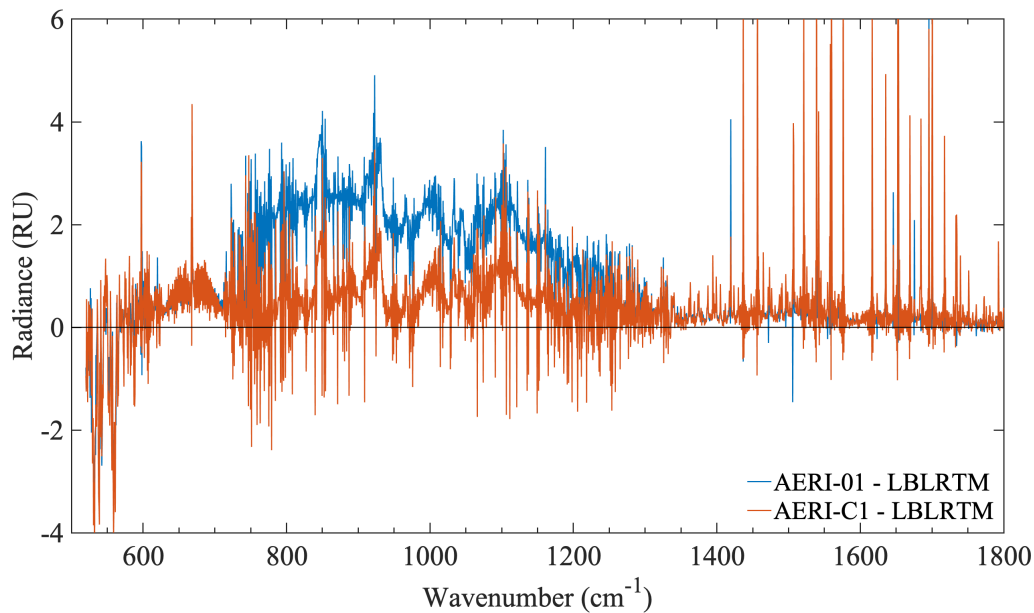607 closures between observation and simulation.

608

Figure B3. The clear sky monthly mean difference between AERI observations and LBLRTM simulations in October 2006.

We originally used the ozone concentration profile from the Modern-Era Retrospective analysis for Research and Applications Version 2 (MERRA-2, Gelaro et al., 2017) in simulating the synthetic spectra. A relatively poorer radiance closure between AERI observations and LBLRTM simulations was found in the ozone absorption band near 1040 cm^{-1}(not shown). By comparing to in situ measurements at SGP (available only at limited times), we find that this is due to poor representation of the local ozone concentration in the MERRA-2 dataset. To address this issue, we vertically scale the ozone profile uniformly to achieve an improved radiance closure in the ozone band as exemplified by Figure B3 (AERI-C1 line), although this has little impact on the all-sky radiance trend detected in Figure 5.

As exemplified in Figure B3, we find that AERI-C1 generally in better agreement with LBLRTM simulations than AERI-01 especially in the window band. The radiance difference in each channel is used to weight the spectra of AERI-01 and AERI-C1, according to Equation (2), to form an integrated record of monthly mean DLR radiance spectra.

References

Clough, S. A., Shephard, M. W., Mlawer, E. J., Delamere, J. S., Iacono, M. J., Cady-Pereira, K., Boukabara, S., & Brown, P. D. (2005). Atmospheric radiative transfer modeling: a summary of the AER codes. *Journal of Quantitative Spectroscopy and Radiative Transfer, 91*(2), 233-244. https://doi.org/10.1016/j.jqsrt.2004.05.058

Cunningham, P., & Delany, S. J. (2020). k-Nearest neighbour classifiers: (with Python examples). *arXiv preprint arXiv:2004.04523.*

Feldman, D. R., Collins, W. D., Gero, P. J., Torn, M. S., Mlawer, E. J., & Shippert, T. R.

635   (2015, Mar 19). Observational determination of surface radiative forcing by CO2

636   from 2000 to 2010. *Nature, 519*(7543), 339-343. https://doi.org/10.1038/nature14240

637

638   Gelaro, R., McCarty, W., Suárez, M. J., Todling, R., Molod, A., Takacs, L., Randles, C. A.,

639   Darmenov, A., Bosilovich, M. G., & Reichle, R. (2017). The modern-era retrospective

640   analysis for research and applications, version 2 (MERRA-2). *Journal of Climate,*

641   *30*(14), 5419-5454.

642

643   Gero, P. J., & Turner, D. D. (2011). Long-Term Trends in Downwelling Spectral Infrared

644   Radiance over the U.S. Southern Great Plains. *Journal of Climate, 24*(18), 4831-4843.

645   https://doi.org/10.1175/2011jcli4210.1

646

647   Harries, J. E., Brindley, H. E., Sagoo, P. J., & Bantges, R. J. (2001). Increases in greenhouse

648   forcing inferred from the outgoing longwave radiation spectra of the Earth in 1970

649   and 1997. *Nature, 410*(6826), 355-357.

650

651   Hersbach, H., Bell, B., Berrisford, P., Hirahara, S., Horányi, A., Muñoz-Sabater, J., Nicolas,

652   J., Peubey, C., Radu, R., & Schepers, D. (2020). The ERA5 global reanalysis.

653   *Quarterly Journal of the Royal Meteorological Society, 146*(730), 1999-2049.

654

655   Holdridge D. 2020. Balloon-Borne Sounding System (SONDE) Instrument Handbook. Ed.

656   by Robert Stafford, U.S. Department of Energy. DOE/SC-ARM/TR-029.

657

658   Huang, Y. (2013). A simulated climatology of spectrally decomposed atmospheric infrared

659   radiation. *Journal of Climate, 26*(5), 1702-1715.

660

661   Huang, Y., Chou, G., Xie, Y., & Soulard, N. (2019). Radiative control of the interannual

662   variability of arctic sea ice. *Geophysical Research Letters, 46*(16), 9899-9908.

663

664   Huang, Y., Leroy, S. S., & Anderson, J. G. (2010). Determining longwave forcing and

665   feedback using infrared spectra and GNSS radio occultation. *Journal of Climate,*

666   *23*(22), 6027-6035.

667

668 Huang, Y., & Ramaswamy, V. (2009). Evolution and Trend of the Outgoing Longwave
669   Radiation Spectrum. *Journal of Climate, 22*(17), 4637-4651.
670   https://doi.org/10.1175/2009jcli2874.1
671
672 Huang, Y., Ramaswamy, V., Huang, X., Fu, Q., & Bardeen, C. (2007). A strict test in climate
673   modeling with spectrally resolved radiances: GCM simulation versus AIRS
674   observations. *Geophysical Research Letters, 34*(24).
675   https://doi.org/10.1029/2007gl031409
676
677 Huang, Y., Ramaswamy, V., & Soden, B. (2007). An investigation of the sensitivity of the
678   clear-sky outgoing longwave radiation to atmospheric temperature and water vapor.
679   *Journal of Geophysical Research, 112*(D5). https://doi.org/10.1029/2005jd006906
680
681 Jacobson, A. R., Schuldt, K. N., Miller, J. B., Oda, T., Tans, P., Arlyn, A., Mund, J., Ott, L.,
682   Collatz, G. J., Aalto, T., Afshar, S., Aikin, K., Aoki, S., Apadula, F., Baier, B.,
683   Bergamaschi, P., Beyersdorf, A., Biraud, S. C., Bollenbacher, A., Bowling, D.,
684   Brailsford, G., Abshire, J. B., Chen, G., Huilin, C., Lukasz, C., Sites, C., Colomb, A.,
685   Conil, S., Cox, A., Cristofanelli, P., Cuevas, E., Curcoll, R., Sloop, C. D., Davis, K.,
686   Wekker, S. D., Delmotte, M., DiGangi, J. P., Dlugokencky, E., Ehleringer, J., Elkins,
687   J. W., Emmenegger, L., Fischer, M. L., Forster, G., Frumau, A., Galkowski, M., Gatti,
688   L. V., Gloor, E., Griffis, T., Hammer, S., Haszpra, L., Hatakka, J., Heliasz, M.,
689   Hensen, A., Hermanssen, O., Hintsa, E., Holst, J., Jaffe, D., Karion, A., Kawa, S. R.,
690   Keeling, R., Keronen, P., Kolari, P., Kominkova, K., Kort, E., Krummel, P., Kubistin,
691   D., Labuschagne, C., Langenfelds, R., Laurent, O., Laurila, T., Lauvaux, T., Law, B.,
692   Lee, J., Lehner, I., Leuenberger, M., Levin, I., Levula, J., Lin, J., Lindauer, M., Loh,
693   Z., Lopez, M., Luijkx, I. T., Myhre, C. L., Machida, T., Mammarella, I., Manca, G.,
694   Manning, A., Manning, A., Marek, M. V., Marklund, P., Martin, M. Y., Matsueda, H.,
695   McKain, K., Meijer, H., Meinhardt, F., Miles, N., Miller, C. E., Mölder, M., Montzka,
696   S., Moore, F., Josep-Anton, M., Morimoto, S., Munger, B., Jaroslaw, N., Newman, S.,
697   Nichol, S., Niwa, Y., O'Doherty, S., Mikaell, O.-L., Paplawsky, B., Peischl, J., Peltola,
698   O., Jean-Marc, P., Piper, S., Plass-Dölmer, C., Ramonet, M., Reyes-Sanchez, E.,
699   Richardson, S., Riris, H., Ryerson, T., Saito, K., Sargent, M., Sasakawa, M., Sawa, Y.,
700   Say, D., Scheeren, B., Schmidt, M., Schmidt, A., Schumacher, M., Shepson, P.,

701   Shook, M., Stanley, K., Steinbacher, M., Stephens, B., Sweeney, C., Thoning, K.,

702   Torn, M., Turnbull, J., Tørseth, K., Bulk, P. V. D., Dinther, D. V., Vermeulen, A.,

703   Viner, B., Vitkova, G., Walker, S., Weyrauch, D., Wofsy, S., Worthy, D., Dickon, Y., &

704   Miroslaw, Z. (2020). *CarbonTracker CT2019B*.

705   https://www.esrl.noaa.gov/gmd/ccgg/carbontracker/CT2019B/

706

707   Kapsch, M.-L., Graversen, R. G., Tjernström, M., & Bintanja, R. (2016). The effect of

708   downwelling longwave and shortwave radiation on Arctic summer sea ice. *Journal of*

709   *Climate, 29*(3), 1143-1159.

710

711   Knuteson, R., Revercomb, H., Best, F., Ciganovich, N., Dedecker, R., Dirkx, T., Ellington, S.,

712   Feltz, W., Garcia, R., & Howell, H. (2004a). Atmospheric emitted radiance

713   interferometer. Part I: Instrument design. *Journal of Atmospheric and Oceanic*

714   *Technology, 21*(12), 1763-1776.

715

716   Knuteson, R., Revercomb, H., Best, F., Ciganovich, N., Dedecker, R., Dirkx, T., Ellington, S.,

717   Feltz, W., Garcia, R., & Howell, H. (2004b). Atmospheric emitted radiance

718   interferometer. Part II: Instrument performance. *Journal of Atmospheric and Oceanic*

719   *Technology, 21*(12), 1777-1789.

720

721   Liebmann, B., & Smith, C. A. (1996). Description of a complete (interpolated) outgoing

722   longwave radiation dataset. *Bulletin of the American Meteorological Society, 77*(6),

723   1275-1277.

724

725   Lubin, D. (1994). The role of the tropical super greenhouse effect in heating the ocean

726   surface. *Science, 265*(5169), 224-227.

727

728   Peters, W., Jacobson, A. R., Sweeney, C., Andrews, A. E., Conway, T. J., Masarie, K., Miller,

729   J. B., Bruhwiler, L. M., Pétron, G., & Hirsch, A. I. (2007). An atmospheric

730   perspective on North American carbon dioxide exchange: CarbonTracker.

731   *Proceedings of the National Academy of Sciences, 104*(48), 18925-18930.

732

733   Revercomb, H. E., Buijs, H., Howell, H. B., LaPorte, D. D., Smith, W. L., & Sromovsky, L.

734   (1988). Radiometric calibration of IR Fourier transform spectrometers: solution to a

735   problem with the High-Resolution Interferometer Sounder. *Applied Optics, 27*(15),

736   3210-3218.

737

738   Revercomb, H. E., Turner, D. D., Tobin, D., Knuteson, R. O., Feltz, W., Barnard, J.,

739   Bösenberg, J., Clough, S., Cook, D., & Ferrare, R. (2003). The ARM program's water

740   vapor intensive observation periods: Overview, initial accomplishments, and future

741   challenges. *Bulletin of the American Meteorological Society, 84*(2), 217-236.

742

743   Rowe, P. M., Neshyba, S. P., Cox, C. J., & Walden, V. P. (2011). A responsivity-based

744   criterion for accurate calibration of FTIR emission spectra: identification of in-band

745   low-responsivity wavenumbers. *Optics express, 19*(7), 5930-5941.

746

747   Rowe, P. M., Neshyba, S. P., & Walden, V. P. (2011). Responsivity-based criterion for

748   accurate calibration of FTIR emission spectra: theoretical development and bandwidth

749   estimation. *Optics express, 19*(6), 5451-5463.

750

751   Shupe, M. D., & Intrieri, J. M. (2004). Cloud Radiative Forcing of the Arctic Surface: The

752   Influence of Cloud Properties, Surface Albedo, and Solar Zenith Angle. *Journal of

753   Climate, 17*(3), 616-628. https://doi.org/10.1175/1520-

754   0442(2004)017<0616:Crfota>2.0.Co;2

755

756   Sokolowsky, G. A., Clothiaux, E. E., Baggett, C. F., Lee, S., Feldstein, S. B., Eloranta, E. W.,

757   Cadeddu, M. P., Bharadwaj, N., & Johnson, K. L. (2020). Contributions to the Surface

758   Downwelling Longwave Irradiance during Arctic Winter at Utqiaġvik (Barrow),

759   Alaska. *Journal of Climate, 33*(11), 4555-4577. https://doi.org/10.1175/jcli-d-18-

760   0876.1

761

762   Stephens, G. L., Li, J., Wild, M., Clayson, C. A., Loeb, N., Kato, S., L'Ecuyer, T.,

763   Stackhouse, P. W., Lebsock, M., & Andrews, T. (2012). An update on Earth's energy

764   balance in light of the latest global observations. *Nature Geoscience, 5*(10), 691-696.

765   https://doi.org/10.1038/ngeo1580

766

767   Tiao, G. C., Reinsel, G. C., Xu, D., Pedrick, J., Zhu, X., Miller, A., DeLuisi, J., Mateer, C., &
768   Wuebbles, D. (1990). Effects of autocorrelation and temporal sampling schemes on
769   estimates of trend and spatial correlation. *Journal of Geophysical Research:*
770   *Atmospheres, 95*(D12), 20507-20517.

772   Trenberth, K. E., Fasullo, J. T., & Kiehl, J. (2009). Earth's Global Energy Budget. *Bulletin of*
773   *the American Meteorological Society, 90*(3), 311-324.
774   https://doi.org/10.1175/2008bams2634.1

776   Turner, D., Knuteson, R., Revercomb, H., Lo, C., & Dedecker, R. (2006). Noise reduction of
777   Atmospheric Emitted Radiance Interferometer (AERI) observations using principal
778   component analysis. *Journal of Atmospheric and Oceanic Technology, 23*(9), 1223-
779   1238.

781   Turner, D. D., & Gero, P. J. (2011). Downwelling 10μm radiance temperature climatology for
782   the Atmospheric Radiation Measurement Southern Great Plains site. *Journal of*
783   *Geophysical Research, 116*(D8). https://doi.org/10.1029/2010jd015135

785   Turner, D. D., Lesht, B. M., Clough, S. A., Liljegren, J. C., Revercomb, H. E., & Tobin, D.
786   (2003). Dry bias and variability in Vaisala RS80-H radiosondes: The ARM
787   experience. *Journal of Atmospheric and Oceanic Technology, 20*(1), 117-132.

789   Turner, D. D., Tobin, D., Clough, S. A., Brown, P. D., Ellingson, R. G., Mlawer, E. J.,
790   Knuteson, R. O., Revercomb, H. E., Shippert, T. R., & Smith, W. L. (2004). The QME
791   AERI LBLRTM: A closure experiment for downwelling high spectral resolution
792   infrared radiance. *Journal of the atmospheric sciences, 61*(22), 2657-2675.

794   Wang, J., Cole, H. L., Carlson, D. J., Miller, E. R., Beierle, K., Paukkunen, A., & Laine, T. K.
795   (2002). Corrections of humidity measurement errors from the Vaisala RS80
796   radiosonde—Application to TOGA COARE data. *Journal of Atmospheric and*
797   *Oceanic Technology, 19*(7), 981-1002.

799   Weatherhead, E. C., Reinsel, G. C., Tiao, G. C., Meng, X.-L., Choi, D., Cheang, W.-K.,

800   Keller, T., DeLuisi, J., Wuebbles, D. J., Kerr, J. B., Miller, A. J., Oltmans, S. J., &

801   Frederick, J. E. (1998). Factors affecting the detection of trends: Statistical

802   considerations and applications to environmental data. *Journal of Geophysical*

803   *Research: Atmospheres, 103*(D14), 17149-17161. https://doi.org/10.1029/98jd00995

804

805 Wielicki, B. A., Wong, T., Allan, R. P., Slingo, A., Kiehl, J. T., Soden, B. J., Gordon, C.,

806   Miller, A. J., Yang, S.-K., & Randall, D. A. (2002). Evidence for large decadal

807   variability in the tropical mean radiative energy budget. *Science, 295*(5556), 841-844.

808

809 Wild, M., Folini, D., Schär, C., Loeb, N., Dutton, E. G., & König-Langlo, G. (2012). The

810   global energy balance from a surface perspective. *Climate Dynamics, 40*(11-12),

811   3107-3134. https://doi.org/10.1007/s00382-012-1569-8

812

813